X-ray diffraction on laterally modulated $(InAs)_n/(AlAs)_m$ short-period superlattices

O. Caha and V. Křápek
Institute of Condensed Matter Physics, Masaryk University, Kotlářská 2, 61137 Brno, Czech Republic

V. Holý
Department of Physics of Electronic Structures, Charles University, Ke Karlovu 5, 121 16 Prague, Czech Republic

S. C. Moss and J. H. Li
Physics Department and Texas Center for Superconductivity and Advanced Materials, University of Houston, Houston, Texas 77204-5005

A. G. Norman and A. Mascarenhas
National Renewable Energy Laboratory, Golden, Colorado 80401

J. L. Reno
Physical and Chemical Science Center, Sandia National Laboratories, Albuquerque, New Mexico 87185

J. Stangl and M. Meduňa
Institut für Halbleiterphysik, Johannes Kepler Universität, A-4040 Linz, Austria

(Received 24 March 2004; accepted 14 June 2004)

Lateral composition modulation in InAs/AlAs short-period superlattices was investigated by x-ray grazing-incidence diffraction and coplanar x-ray diffraction at a "normal" wavelength and at an anomalous wavelength, for which diffraction from the (200) planes does not exhibit a chemical contrast. The experimental data were compared with theoretical simulations assuming that the interfaces consist of a periodic sequence of monoatomic steps. The displacement field in the superlattice was calculated by continuum elasticity and using a valence-force field method. From the fit of the experimental data to the theory, the lengths of individual atomic terraces were determined. © *2004 American Institute of Physics*. [DOI: 10.1063/1.1781768]

I. INTRODUCTION

During growth of short-period superlattices (SPS), spontaneous lateral composition modulation (LCM) can occur leading to a quasiperiodic modulation of the thicknesses of individual layers; resulting one-dimensional nanostructures (quantum wires) have potential applications in optoelectronics. LCM was observed in several types of SPS's based on III-V systems, such as InAs/AlAs on InP(001)[1] or InP/GaP on GaAs(001).[2] The origin of the composition modulation is not fully understood yet; it is a subject of extensive theoretical investigations; see Refs. 3 and 4, among others.

Lateral composition modulation in an AlAs/InAs SPS has been studied so far by transmission electron microscopy (TEM),[5] atomic force microscopy,[6] photoluminescence[7,8] and x-ray diffraction (XRD).[9] In these works it was found that the modulation can occur in various azimuthal directions,[5,6] depending on the mean composition of the InAs/AlAs superlattice. In superlattices with thicker InAs layers, a modulation towards ⟨100⟩ is preferred, while, Al-rich superlattices are modulated along ⟨310⟩.[10]

This paper represents a continuation of our investigations published previously,[9,11] in which high-resolution x-ray scattering experiments in laterally modulated InAs/AlAs SPS's were analyzed, assuming a sinuslike form of the interfaces. However, the actual form of the interfaces substantially differs from this simplified shape, since the interface consists of a sequence of discrete monolayer steps. In the present paper, we improve the structure model of a modulated SPS taking this discrete nature of the interfaces into account. We use a discrete model of the interfaces for the analysis of XRD data taken both in coplanar and grazing-incidence geometry (GID).

A substantial step in the analysis of x-ray diffraction data is a simulation of the elastic strain fields caused by the lattice mismatch between the constituting layers, and affected by the local interface profile. For this calculation, we use continuum elasticity (CE)[11,12] and valence force field (VFF) methods.[13] The application of the VFF method for a system with a free surface is complicated, since one has to take into account free dangling bonds and a surface reconstruction. Therefore, in order to simplify the calculations, we restrict the application of VFF only to an infinite superlattice. On the other hand, the CE approach is based on an analytic solution of continuum elasticity equations and it can be used also in a close vicinity of the surface. Showing that the results of both methods coincide with a good precision far from the surface, we confirm the general validity of the CE method, which was eventually used for the simulation of scattering measurements.

The paper is organized as follows. X-ray experiments are described in the following section; Sec. III deals with the

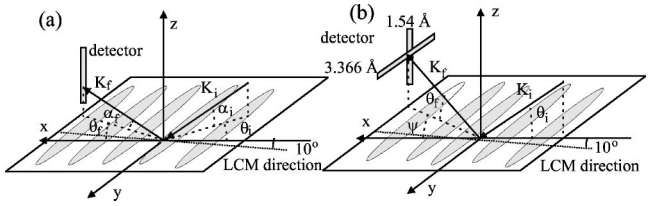

FIG. 1. Experimental setup of the GID (a) HAD (b) geometries. The *x* and *y* axes are parallel to [100] and [010], respectively. The *z* axis is parallel to the growth direction (close to [001]). The gray stripes denote the orientation of quantum wires produced by LCM.

methods of strain calculation in modulated SPS's; the comparison of the measured diffraction data with the theory is presented in Sec. IV.

II. EXPERIMENTS

The sample named EA0532 was investigated already in our previous works.[9,11] The sample was grown by molecular beam epitaxy at 545 °C and using the deposition rate of 0.35 ML/sec,[9] where ML stands for monolayer. The superlattice contains 100 InAs/AlAs periods; the nominal thicknesses of InAs and AlAs layers are 1.9 and 1.5 monolayers. The superlattice stack is deposited on a 100 nm thick buffer layer of In_nAl_mAs grown on InP(001); the buffer layer has the same chemical composition as the average composition of the SPS. Thus, the SPS as a whole is lattice matched to the buffer layer and no misfit dislocations in the SPS are present, which was confirmed by TEM.[1,14] An important parameter determining the LCM type is the substrate miscut; in our sample the miscut angle is $\beta = 1.8 \pm 0.2°$ and the azimuthal direction of the miscut is inclined from [100] by about 10°. The direction of the LCM exactly coincides with the miscut direction. The period of the LCM was determined from TEM to $L = 280 \pm 10$ Å.

The x-ray experiments were performed at the ID10B beamline at ESRF, Grenoble, using the wavelength $\lambda = 1.54$ Å and at the ID01 beamline at ESRF using the anomalous wavelength $\lambda = 3.366$ Å. At the latter wavelength, AlAs and InAs have the same polarizabilities in diffraction from (200) planes and therefore, the diffracted intensity depends only on the elastic deformation field in the sample and not on the chemical composition. The experiments were performed GID and in a nearly coplanar XRD geometry, sketched schematically in Fig. 1. In both cases, a linear position-sensitive x-ray detector (PSD) was used.

The GID 200 diffraction at 3.366 Å was measured with the PSD oriented perpendicular to the surface, so that one PSD scan represents the dependence of the scattered intensity on the exit angle α_f. In this diffraction, the in-plane component of the (200) diffraction vector was parallel to the LCM direction. The reciprocal space map with the incidence angle $\alpha_i = 0.5°$, and the penetration depth of 90 Å in the coordinates Q_xQ_z is plotted in Fig. 2(a), the Q_x axis is parallel to the in-plane component of the diffraction vector (see Fig. 1—radial axis). Nearly periodic LCM gives rise to lateral intensity satellites along the LCM direction. Due to local differences in the LCM direction and an azimuthal divergence of the primary beam, the lateral satellites are slightly

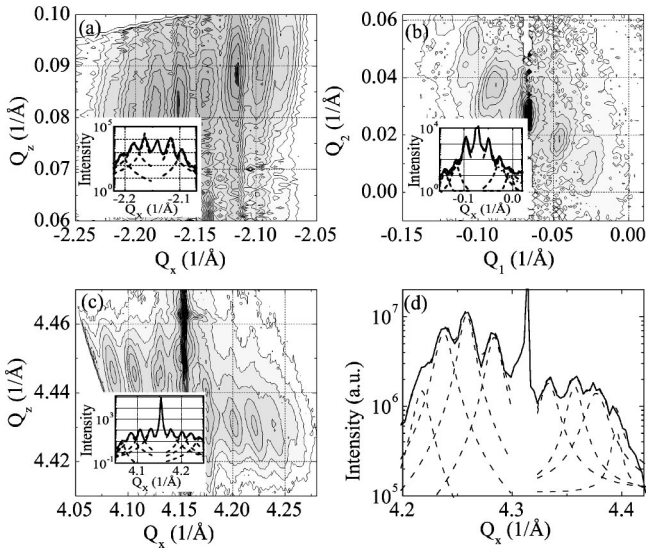

FIG. 2. Measured reciprocal-space intensity maps and extracted cuts through the lateral maxima with fitted Lorentzian profiles (insets): (a) GID 200 at $\lambda = 3.366$ Å, (b) XRD 002 at $Q_z = 2.136$ Å^{-1} using $\lambda = 3.366$ Å; Q_1 and Q_2 are parallel to [110] and [1–10], respectively, (c) XRD 404 at $\lambda = 1.54$ Å, (d) line scan extracted from three-dimensional map XRD 400 at $\lambda = 1.54$ Å. In the maps, the step of the intensity contours is $10^{1/3}$.

smeared along Q_y and it was possible to detect the satellites even for a LCM direction misoriented from [100]; up to the ±3rd-order satellites are visible. Very similar results were obtained for the incidence angle $\alpha_i = 0.7°$, corresponding to the penetration depth of about 500 Å. This demonstrates a nearly full vertical homogeneity of the superlattice.

In the XRD experiments at $\lambda = 3.366$ Å, the PSD was parallel to the sample surface (Fig. 1). This arrangement made it possible to measure a two-dimensional intensity distribution in a reciprocal plane $Q_z = \text{const}$ parallel to the sample surface. The reciprocal-intensity map was reconstructed from a series of ψ-scans taken for various azimuthal directions of the primary x-ray beam. Three maps at different Q_z's were measured around the symmetrical 002 reciprocal lattice point. In Fig. 2(b), only the map at $Q_z = 2.136$ Å^{-1} is plotted, the other maps measured at $Q_z = 2.12$ Å^{-1} and 2.15 Å^{-1} are very similar; this confirms again the vertical homogeneity of the sample. In these intensity maps, the lateral satellites can be resolved up to the order of ±3.

Using $\lambda = 1.54$ Å and the GID geometry, we have measured a full three-dimensional intensity map around 400 reciprocal lattice point with the penetration depth of about 210 Å, using a PSD perpendicular to the sample surface. The measurement procedure is described in our previous work.[11] In Fig. 2(d) is shown only an extracted line scan through the lateral maxima. In the map, the satellites up to the order ±4 are visible. The measurement was performed only to find the exact direction of the LCM modulation.

The XRD measurement at the same wavelength (1.54 Å) was performed in the usual setting with the PSD detector perpendicular to the sample surface. This arrangement made it possible to measure the intensity distribution in a vertical reciprocal plane around the asymmetric reciprocal lattice point 404 [Fig. 2(c)]. In XRD geometries with both wavelengths, the penetration depth exceeded the total superlattice thickness.

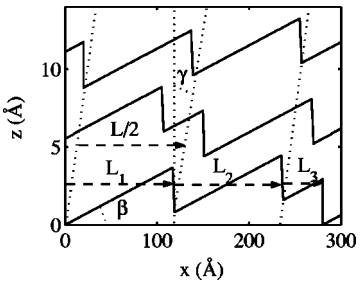

FIG. 3. The structure model of interfaces in the superlattice. L is the LCM period along x axis, L_1, L_2, L_3 are the terrace lengths, γ is the replication angle, and β is the miscut angle.

The scattered intensity was detected as a function of the scattering vector $\mathbf{Q}=\mathbf{K}_f-\mathbf{K}_i$, where $\mathbf{K}_{i,f}$ are the wave vectors of incident and scattered beams, respectively. In GID, changing the angle of incidence α_i, we tune the penetration depth of the incoming radiation, so that we can suppress the scattering in the substrate.

From the intensity maps measured both in the GID and XRD geometries, the mean period of the LCM was determined to $L=(280\pm10)$Å, which agrees well with TEM observations.[14] From the Q_xQ_z intensity maps in Fig. 2 it is obvious that the row of the lateral satellites is *not* parallel to the sample surface. The profiles of different interfaces in the SPS are replicated; the replication direction is always perpendicular to the row of the satellites in the Q_xQ_z plane. In our case, the replication direction is tilted by $\gamma=(4\pm1)°$ off the growth direction; the azimuthal direction of this tilt is the same as that of the LCM.

III. CALCULATION OF THE DISPLACEMENT FIELD

For the calculation of the elastic displacement field in a SPS with a lateral modulation, we have used a model of monoatomic stairs (Fig. 3). From the mean LCM period L and the miscut angle $\beta=1.8\pm0.2°$ it follows that three monoatomic steps (and three atomically flat terraces) fit in one LCM period; the widths of these terraces averaged over many LCM periods are denoted $L_{1,2,3}$. The obvious relation $L_1+L_2+L_3=L$ holds.

We assume that all the interfaces in the SPS stack have the same values of $L_{1,2,3}$. The positions of the steps at equivalent interfaces are laterally shifted according to the replication angle γ determined from the experimental data. The sequence of the terraces at adjacent InAs/AlAs and AlAs/InAs interfaces are shifted laterally by $L/2$; this shift leads to a lateral modulation of the average chemical composition of the SPS. The structure model is schematically sketched in Fig. 3, where all the model parameters, namely $L_{1,2,3}, \beta, \gamma$, are explained.

A. Continuum elasticity method

The method is based on the approach published previously in Refs. 11 and 12, based on the analytic solution of the elastic equilibrium equations,

$$\frac{\partial \sigma_{jk}}{\partial x_k}+f_j=0, \quad j,k=1,2,3, \tag{1}$$

where σ_{jk} are the components of the stress tensor,

$$f_j=-(C_{11}+2C_{12})\frac{\partial \delta(\mathbf{x})}{\partial x_j} \tag{2}$$

is the jth component of the density of the volume force, C_{11}, C_{12} are elastic constants, and $\delta(\mathbf{x})$ is the local lattice mismatch with respect to the substrate (InP) in the point $\mathbf{x}=(x_1,x_2,x_3)$. We assume a flat surface with the boundary conditions

$$\sigma_{jk}|_{\text{surface}} n_k=0, \tag{3}$$

where n_k is kth component of the surface normal. We have also assumed that (i) the elastic constants do not depend on the chemical composition, (ii) the modulation is perfectly periodic in the direction $x\|[100]$, and (iii) the sample structure is completely homogeneous along $y\|(010)$ (i.e., along the monoatomic steps). Then, due to the cubic symmetry of the matrix C_{jk} of the elastic constants, the displacement field has only two nonzero components u_x, u_z, depending only on the coordinates $x\equiv x_1$ (parallel to the surface and to the LCM direction) and $z\equiv x_3$ (parallel to the *outward* surface normal).

Assuming a perfect periodicity in x with the period L, we can express the displacement field as the Fourier series,

$$\mathbf{u}(x,z)=\sum_k \mathbf{u}^{FT}(k,z)e^{ikx}, \tag{4}$$

where k is an integer multiple of $2\pi/L$. Putting from Eq. (4) into Eqs. (1) and (3), we obtain a system of ordinary differential equations,

$$\hat{\mathbf{A}}\frac{d^2}{dz^2}\mathbf{u}^{FT}+i\hat{\mathbf{B}}\frac{d}{dz}\mathbf{u}^{FT}-\hat{\mathbf{C}}\mathbf{u}^{FT}=\mathbf{P}, \tag{5}$$

where

$$\hat{\mathbf{A}}=\begin{pmatrix} C_{44} & 0 \\ 0 & C_{11}\end{pmatrix},$$

$$\hat{\mathbf{B}}(k)=\begin{pmatrix} 0 & k(C_{12}+C_{44}) \\ k(C_{12}+C_{44}) & 0\end{pmatrix}, \tag{6}$$

$$\hat{\mathbf{C}}(k)=\begin{pmatrix} k^2C_{11} & 0 \\ 0 & k^2C_{44}\end{pmatrix},$$

and

$$\mathbf{u}^{FT}(k,z)=\begin{pmatrix} u_x(k,z) \\ u_z(k,z)\end{pmatrix},$$

$$\mathbf{P}(k,z)=(C_{11}+2C_{12})\begin{pmatrix} ik\delta^{FT}(k,z) \\ d/dz\ \delta^{FT}(k,z)\end{pmatrix}. \tag{7}$$

The one-dimensional Fourier transform of the local mismatch $\delta(x,z)$ with respect to x is denoted as $\delta^{FT}(k,z)$. The boundary conditions for $\mathbf{u}^{FT}$ at the free surface and in the substrate far below the superlattice are

$$\hat{\mathbf{A}}\frac{d}{dz}\mathbf{u}^{FT} + i\hat{\mathbf{D}}\mathbf{u}^{FT}|_{z=0,z\to-\infty} = 0, \tag{8}$$

where

$$\hat{\mathbf{D}} = \begin{pmatrix} 0 & kC_{44} \\ kC_{12} & 0 \end{pmatrix}. \tag{9}$$

Equation (5) can be analytically solved finding the general solution of the homogenous equation

$$\hat{\mathbf{A}}\frac{d^2}{dz^2}\mathbf{u}^{FT} + i\hat{\mathbf{B}}\frac{d}{dz}\mathbf{u}^{FT} - \hat{\mathbf{C}}\mathbf{u}^{FT} = 0 \tag{10}$$

and one particular solution of the full equation. Details of the procedure can be found elsewhere.[12]

B. Valence-force field method

The VFF method is based on the minimization of the total energy of the crystal. This energy is expressed by means of an interatomic potential depending on the mutual positions of pairs and triplets of neighboring atoms. Several empirical or semiempirical interatomic potentials have been used in the literature, we have chosen the potential obtained by Keating,[15] and extended by Martin[13] for zinc-blende structures,

$$V = \frac{1}{2}\sum_i \left[\frac{1}{4}\sum_{j=1}^{4} \frac{\alpha_{ij}}{a_{ij}^2}(\mathbf{v}_{ij}{}^2 - 3a_{ij}^2)^2 + \frac{1}{2}\sum_{j=1,k>j}^{4} \frac{\beta_{ijk}}{a_{ij}a_{ik}}(v_{ij}\cdot\mathbf{v}_{ik} + a_{ij}a_{ik})^2 \right], \tag{11}$$

where α_{ij}, β_{ijk} are potential constants, $\mathbf{v}_{ij}$ denotes the vector connecting the ith and the jth atoms, and a_{ij} is $\frac{1}{4}$ of the lattice parameter. The sum over i runs over all atoms in the system, the sums over j and k comprise only four nearest neighbors of the atom i. The first term in the expression expresses the bond length change from the strain-free state, the second describes the change in the bond angles.

Minimizing the total energy in Eq. (11), we obtain a system of $3N$ cubic equations, where N is the total number of atoms in the system. Direct solution of the system is impossible and we used a numerical approach described in Ref. 16; the method consists in the following. In each computation step, we minimize the energy, allowing one single atom to deviate from its starting position, other atoms are held fixed. One iteration step consists in a sequence of N computation steps, i.e., in a subsequent finding of the optimum positions of all N atoms. The iteration steps are repeated until the maximum change in the atomic positions between two last iteration steps is smaller than a requested accuracy.

In order to simplify the model, in the application of VFF we have restricted to an *infinite* periodic multilayer and we have *not* included the surface. Therefore, the results of the calculation do not consider both the surface relaxation and the influence of the substrate, and they can be compared with the results of the CE method (see above) only far below the sample surface and far from the substrate interface.

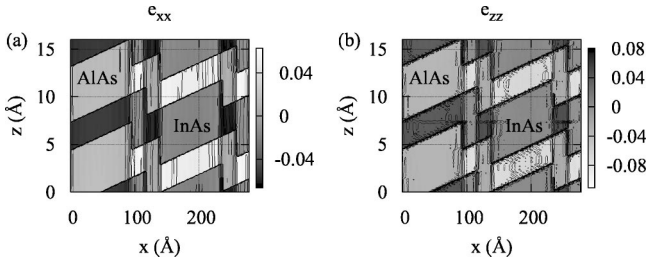

FIG. 4. ϵ_{xx} and ϵ_{zz} components of the strain tensor. Zero strain corresponds to a nondeformed layer material. Contour step is 1%, almost all contours are on the layer intrerfaces.

C. Comparison of the CE and the VFF methods

The components of the strain tensor,

$$\epsilon_{j,k} = \frac{1}{2}\left(\frac{\partial u_j}{\partial x_k} + \frac{\partial u_k}{\partial x_j}\right), \quad x_{j,k} = x,z; u_{j,k} = u_x,u_z,$$

obtained by the CE method are plotted in Fig. 4. From the figures it is obvious that the strain field in the SPS, averaged vertically and laterally over the SPS and LCM periods, is homogeneous except for ≈5 nm thin regions at the free surface and at the substrate interface.

We compared the results of CE and VFF in the region of the homogeneous deformation; Fig. 5 presents the displacement components $u_{x,z}$ in one bilayer calculated by both methods. The maximum difference in u_x and u_z is about 0.14 Å and 0.095 Å, respectively. The corresponding relative difference in u_x is about 6.5 %; since u_z is rather small (below ≈0.5 Å), this small difference in u_z makes relatively about 26%.

The differences in the displacement components obtained by CE and VFF methods are caused by different approximations used. The CE method approximates the actual crystal lattice by a continuum. The error introduced by this continuum approach is substantial, if the smallest size of the structure details is comparable to the lattice parameter. This is the case for the thicknesses of individual layers; the LCM period, on the other hand, is much larger. Therefore, the continuum approximation affects the values of u_z rather than u_x. Other important approximation made in the CE method is the independence of the elastic constants on the chemical composition. In addition, the CE method assumes a linear elasticity, i.e., the elastic energy in the continuum approximation is proportional to the square of the displacements, whereas

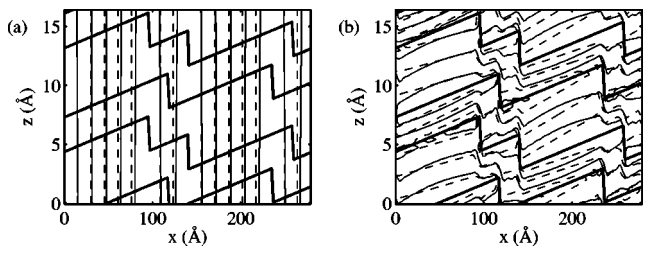

FIG. 5. Contours of the u_x (a) and u_z (b) components of the displacement field, defined with respect to the InP substrate lattice, computed by the CE (solid lines) and by the VFF methods (dashed lines). Contour steps are 0.35 Å and 0.9 Å in panels (a) and (b), respectively. Thick lines denote the interfaces between the InAs and AlAs layers.

the interatomic potential in Eq. (11) contains the fourth powers of the displacements. For the actual mismatch values, however, the nonlinearity plays a minor role. Moreover, the VFF method considers the true point symmetry T_d of the zinc-blende unit cell, whereas the matrix of the elastic constants C_{jk} exhibits a higher O_h cubic symmetry. This difference, however, can be ruled out for the LCM orientation [100].

We have studied the influence of these differences to the simulated x-ray diffraction intensities (see Sec. IV). We calculated the intensities of the lateral maxima according to Eq. (12) from the displacement field obtained by the CE and the VFF methods; in all geometries and wavelengths used in our study, the relative difference in the satellite intensities obtained by these methods do not exceed 10%; this difference is smaller than the smallest difference achieved between the measured and simulated diffraction data.

IV. SIMULATION OF X-RAY DIFFRACTION

The diffracted intensity was calculated by means of the distorted-wave Born approximation.[17,18] The scattering vector $\mathbf{Q}=\mathbf{K_f}-\mathbf{K_i}$ was corrected to refraction $\mathbf{Q}_T=\mathbf{k}_f-\mathbf{k}_i$, where $\mathbf{k}_{i,f}$ are the refraction-corrected wave vectors of the primary and scattered beams, respectively. The refraction correction comprises also absorption, thus, the z components of these vectors are complex. The scattered intensity is given by the expression[12]

$$I(\mathbf{Q}) = \text{const}|t_i t_f|^2 \left| \int \chi_{\mathbf{h}}(\mathbf{r}) e^{-i\mathbf{h}\cdot\mathbf{u}(\mathbf{r})} e^{-i\mathbf{q}\cdot\mathbf{r}} d^3\mathbf{r} \right|^2,$$
$$\mathbf{q} = \mathbf{Q}_T - \mathbf{h}, \tag{12}$$

where $\mathbf{h}$ is the reciprocal lattice vector (diffraction vector) defined with respect to the lattice reciprocal to the mean lattice of the SPS. t_i, t_f are the transmission coefficients of the surface for the primary and the scattered wave, respectively, and $\chi_{\mathbf{h}}(\mathbf{r})$ is the $\mathbf{h}$th Fourier coefficient of crystal polarizability. This coefficient depends on the coordinates (x,z), due to the local chemical composition in the sample.

Assuming a perfectly periodic structure along x, the scattered intensity consists of a periodic sequence of δ-like peaks (intensity satellites) in the positions $q_{xp}=p(2\pi)/L$, where p is an integer. In an experimental reciprocal-space map, the peaks are smeared, due to a limited experimental resolution in reciprocal space and due to random deviations from the periodicity of the LCM. If the deviations obey a short-range-order model, in the first approximation, they do not change the integrated intensities of the satellites. Therefore, we have compared the integrated intensities of the measured lateral satellites with the satellite intensities calculated assuming a perfectly periodic LCM.

The vertical periodicity of the SPS gives rise to superlattice satellites along the Q_z axis. All our measurements were performed around the zero-order superlattice satellite, thus for $\text{Re}(q_z)\approx 0$. Then the intensity of the jth lateral satellite is proportional to the square of the jth coefficient in the Fourier series of $\chi(\mathbf{x})\exp[-i\mathbf{h}\cdot\mathbf{u}(\mathbf{x})]$ along x. Since the diffraction vector $\mathbf{h}$ in the GID arrangements is nearly parallel to the sample surface, only the u_x component affects the scattered intensity in this geometry. In contrast, the intensity diffracted in a symmetric coplanar XRD arrangement depends only on u_z. Both components of the displacement field influence the reciprocal-space map measured in an asymmetric XRD setup.

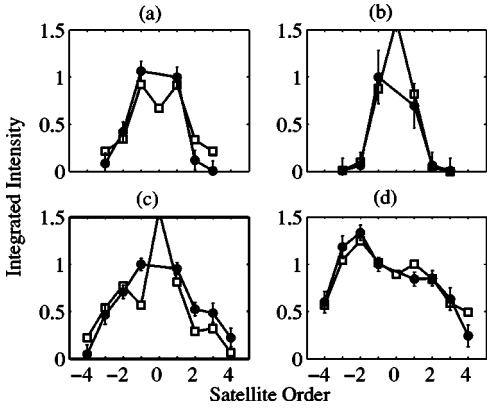

FIG. 6. Comparison of measured (circles) and calculated integrated intensities (squares) of lateral maxima: (a) GID 200 at $\lambda=3.366$ Å, (b) XRD 002 at $\lambda=3.366$ Å, (c) XRD 404 at $\lambda=1.54$ Å, and (d) GID 400 at $\lambda=1.54$ Å.

From the two- and three-dimensional reciprocal-space maps we have extracted linear scans crossing the lateral satellites. Then, we determined the integrated intensities of these satellites by fitting to a periodic sequence of Lorentzian profiles (Fig. 2). From the fit of these integrated intensities to theoretical values calculated using the CE approach, we have determined the widths $L_{1,2,3}$ of the terraces. Both the measured and the fitted integrated intensities of the lateral satellites are plotted in Fig. 6. For the fit we have used the integrated intensities of the satellites measured in GID and XRD around 200 and 002 reciprocal lattice points, using the wavelength 3.366 Å. The resulting terraces length are $L_1=118\pm25$ Å, $L_2=120\pm24$ Å, and $L_3=42\pm30$ Å. We have achieved a fairly good correspondence of experimental and calculated data.

Similar procedure was used for the evaluation of GID and XRD measurements in diffractions 400 and 404, respectively, using the wavelength of 1.54 Å, and we have obtained $L_1=121\pm6$ Å, $L_2=128\pm4$ Å, and $L_3=31\pm7$ Å. The obvious discrepancy between the experimental and calculated integrated intensities in the coplanar 404 diffraction can be ascribed to the fact that, in this case, the penetration depth of the primary beam exceeds the total SPS thickness; most likely, the intensities of the ±1st satellites are affected by the diffuse scattering from defects in the buffer layer under the SPS.

In spite of the anomalous nature of the scattering at 3.366 Å, the experiments at the "usual" wavelength of $\lambda=1.54$ Å are much more sensitive to the terrace lengths. This is due to the following reasons.

(i) The diffraction vector $\mathbf{h}$ in diffraction 400 is 2 times longer than in 200 and 002; in diffraction 404 even 2.8 times. Since, the displacement field $\mathbf{u}(\mathbf{r})$ enters the formula (12) in the scalar product $\mathbf{h}\cdot\mathbf{u}$, the sensitivity of the scattering to the displacement increases with increasing $|\mathbf{h}|$.

(ii) The polarizability at the wavelength 3.366 Å in diffraction 002 (or 200) does not depend on the chemical composition and therefore the chemical contrast is zero. The nonzero chemical contrast at 1.54 Å contributes to the sensitivity of the scattering process to the terrace lengths.

V. DISCUSSION

In Sec. III C we have compared the displacement fields in a short-period laterally modulated superlattice calculated by a CE and VFF methods. Since, in VFF, we have neglected the influence of the free surface and the substrate-SPS interface, this comparison can be performed only in a region far away from these interfaces, where the components of the strain tensor averaged over the superlattice period do not depend on the vertical coordinate z. From this comparison it follows that the CE approach is relevant for the simulation of x-ray diffraction even if the individual layers in the SPS are only few monolayers thick. In Fig. 4 the components ϵ_{xx} and ϵ_{zz} of the strain tensor are plotted; the strain components are defined with respect to the nondeformed material of the particular layer. It is obvious that in the In-rich region (the right half of the figure), the InAs layers are only slightly laterally compressed (less than 1%), while the AlAs layers are in strongly laterally stretched (about 6%) and vertically compressed (about 7%). In the Al-rich regions (the left half of the Fig. 4), the situation is opposite—the AlAs layers are only slightly laterally stretched, while InAs layers are strongly laterally compressed and vertically stretched.

X-ray diffraction intensities were simulated using the CE-calculated displacement field, since the surface relaxation plays a substantial role, especially in GID, where the penetration depth of the primary radiation is comparable to the depth, where the surface relaxation takes place.

The structure model used for the evaluation of experimental data neglects a vertical inhomogeneity of the SPS structure, since we have assumed that all the structure parameters $L_{1,2,3}, \beta, \gamma$ are constant in the superlattice stack. Actually, at the beginning of the superlattice growth, the structure gradually evolves until a stationary growth is reached; this stationary growth mode is observed after the completion of about 10–20 bilayers.[1,10] A possible dispersion of the terrace lengths $L_{1,2,3}$ and local inhomogenities of the LCM period broadens the widths of the lateral satellites, in the first approximation, however, the integrated intensities of the satellites remain unchanged. From the widths of the satellites we can estimate the dispersion of the terrace lengths to (1000 ± 500)Å.

Our results were compared with results in our previous work,[11] where the LCM was modeled by a *continuous* lateral modulation of the mean chemical composition of the SPS. In this paper we found the amplitude of the composition modulation $\Delta x = (16 \pm 0.02)\%$. This result is in a good agreement with the previous work; from the obtained lengths $L_{1,2,3}$ the value $\Delta x = (16 \pm 0.02)\%$ follows.

The consistency of our model is also supported by the agreement of the values of the terrace lengths $L_{1,2,3}$ obtained by means of various scattering geometries using a "normal" and an anomalous wavelength.

VI. CONCLUSION

We have calculated the displacement field in the InAs/AlAs short-period superlattice with laterally modulated thicknesses of individual layers by means of continuum elasticity and a valence-force field method; we have achieved a good coincidence of the results of both methods. Small differences (locally up to 10% in the values of the strain components) were caused by the neglection of the discrete atomistic nature of the superlattice and by the fact that the continuum method neglects the differences in the elasticity constants of constituting materials and nonlinearity effects.

On the basis of simulated elastic displacement field we have calculated x-ray diffraction intensities and compared with experiments performed in several geometries and two different wavelengths. From this comparison we have determined the sizes of the monoatomic terraces constituting the interfaces.

ACKNOWLEDGMENTS

The work was supported by the Grant Agency of Czech Republic (Project No. 202/03/0148) and by the Ministry of Education of Czech Republic (Project No. CEZ 143100002).The synchrotron measurements have been carried out at the beamlines ID10B and ID01 at ESRF, Grenoble; the active assistance of the staffs of these beamlines is highly appreciated.

[1] J. Mirecki Millunchick, R. D. Twesten, D. M. Follstaedt, S. R. Lee, E. D. Jones, Y. Zhang, S. P. Ahrenkiel, and A. Mascarenhas, Appl. Phys. Lett. **70**, 1402 (1997).
[2] K. Y. Cheng, K. C. Hsieh, and J. N. Baillargeon, Appl. Phys. Lett. **60**, 2892 (1992).
[3] L. E. Shilkrot, D. J. Srolovitz, and J. Tersoff, Phys. Rev. B **62**, 8397 (2000).
[4] F. Glas, J. Appl. Phys. **62**, 3201 (1987).
[5] D. M. Follstaedt, R. D. Twesten, J. Mirecki Millunchick, S. R. Lee, E. D. Jones, S. P. Ahrenkiel, Y. Zhang, and A. Mascarenhas, Physica E (Amsterdam) **2**, 325 (1998).
[6] A. G. Norman *et al.*, Appl. Phys. Lett. **73**, 1844 (1998).
[7] E. D. Jones, J. Mirecki Millunchick, D. Follstaedt, S. Lee, J. Reno, R. D. Twesten, Y. Zhang, and A. Mascarenhas, Physica E (Amsterdam) **2**, 44 (1998).
[8] S. Francoer, A. G. Norman, M. C. Hanna, A. Mascarenhas, J. L. Reno, D. M. Follstaedt, and S. R. Lee, Mater. Sci. Eng., B **B88**, 118 (2002).
[9] J. H. Li *et al.*, Appl. Phys. Lett. **78**, 219 (2002).
[10] A. G. Norman *et al.*, Mater. Res. Soc. Symp. Proc. **583**, 297 (2000).
[11] J. H. Li, V. Holý, M. Meduna, S. C. Moss, A. G. Norman, A. Mascarenhas, and J. L. Reno, Phys. Rev. B **66**, 115312 (2002).
[12] T. Roch, V. Holý, A. Hesse, J. Stangl, T. Fromherz, G. Bauer, T. H. Metzger, and S. Ferrer, Phys. Rev. B **65**, 245324 (2002).
[13] R. M. Martin, Phys. Rev. B **1**, 4005 (1970).
[14] C. Dorin, J. Mirecki Millunchick, Y. Chen, B. G. Orr, and C. A. Pearson, Appl. Phys. Lett. **79**, 4118 (2001).
[15] P. N. Keating, Phys. Rev. **145**, 637 (1966).
[16] H. Jiang and J. Singh, Phys. Rev. B **56**, 4696 (1997).
[17] S. K. Sinha, E. B. Sirota, S. Garoff, and H. B. Stanley, Phys. Rev. B **38**, 2297 (1988).
[18] V. Holý, U. Pietsch, and T. Baumbach, *High-Resolution X-ray Scattering from Thin Films and Multilayers* (Springer, Berlin, 1999).